

*Supporting Information for*

**H<sub>2</sub> Evolution by a Cobalt Selenolate Electrocatalyst  
and Related Mechanistic Studies**

Courtney A. Downes, Joseph W. Yoo, Nicholas M. Orchanian, Ralf Haiges, and Smaranda C. Marinescu\*

Department of Chemistry, University of Southern California, Los Angeles, CA, 90089, USA

\*Email: smarines@usc.edu

**General**

All manipulations of air and moisture sensitive materials were conducted under a nitrogen atmosphere in a Vacuum Atmospheres glovebox or on a dual manifold Schlenk line. The glassware was oven-dried prior to use. Water was deionized with the Millipore Synergy system (18.2 MΩ·cm resistivity) and placed under vacuum and refilled with nitrogen (10 ×). Excluding water, all other solvents used were degassed with nitrogen and passed through activated alumina columns and stored over 4Å Linde-type molecular sieves. [Co(bds)<sub>2</sub>][*n*Bu<sub>4</sub>N] (**1**<sup>TBA</sup>) (where bds = 1,2-benzenediselenolate) was synthesized according to literature procedure.<sup>[1]</sup> Proton NMR spectra were acquired at room temperature using a Varian 400-MR 2-Channel spectrometer and referenced to the residual <sup>1</sup>H resonances of the deuterated solvent (<sup>1</sup>H: CD<sub>3</sub>CN, δ 1.94 ppm) All other chemical reagents were purchased from commercial vendors and used without further purification.

**Synthesis of [Co(bds)<sub>2</sub>][PPh<sub>4</sub>] (**1**<sup>TPP</sup>)**

[Co(bds)<sub>2</sub>][PPh<sub>4</sub>] was synthesized following the same literature procedure as **1**<sup>TBA</sup>.<sup>[1]</sup> Tetraphenylphosphonium chloride was used for the cation exchange rather than tetrabutylammonium bromide. Single crystals were grown by slow diffusion of diethyl ether into a methylene chloride solution of [Co(bds)<sub>2</sub>][PPh<sub>4</sub>].

**Synthesis of [Co(bds)<sub>2</sub>][*n*Bu<sub>4</sub>N]<sub>2</sub> (**2**<sup>TBA</sup>)**

KC<sub>8</sub> (9 mg, 0.234 mmol, 6 eq.) was added to a stirred solution of **1**<sup>TBA</sup> (30 mg, 0.039 mmol) in THF at -30°C. The solution was allowed to warm to room temperature and stirred for 3-4 hours, resulting in a color change of the solution from blue to dark yellow. After 4 hours, the solution was filtered and [NBu<sub>4</sub>]Br (25 mg, 0.078 mmol) was added to the dark-yellow filtrate. The mixture was stirred for ~20 hours. The solution was again filtered through a microfiber filter with Celite. The filtrate was evaporated to dryness and recrystallized from a mixture of tetrahydrofuran (THF) and diethyl ether.

**Synthesis of the black precipitate**

Excess [DMF(H)][OTf] or trifluoroacetic acid (TFA) was added to a solution of **1** in acetonitrile and was stirred overnight. The solution was filtered and the collected black precipitate was washed with acetonitrile and acetone, and dried under vacuum.

### Reduction of the black precipitate

The isolated black precipitate was suspended in DMF and the reaction flask was sealed with a septum. A suspension of excess  $\text{KC}_8$  in DMF was added to the flask via syringe and the mixture was allowed to stir for 30 minutes. Over the course of 30 minutes, the solution turned blue and 2 mL of the headspace of the reaction mixture was injected into the GC confirming  $\text{H}_2$  production.

### Protonation of $[\text{Co}(\text{bds})_2][n\text{Bu}_4\text{N}]_2$ ( $2^{\text{TBA}}$ ) with TFA

A solution of  $2^{\text{TBA}}$  in DMF was added to a round bottom flask and sealed with a septum. Trifluoroacetic acid (1-2 equivalents) was added to the flask via syringe and the reaction mixture was allowed to stir for 30 minutes. Over the course of 30 minutes, the solution turned blue and 2 mL of the headspace of the reaction mixture was injected into the GC confirming  $\text{H}_2$  production.

### Electrochemical Methods

Electrochemistry experiments were carried out using a Pine potentiostat. Cyclic voltammetry experiments were carried out in a single compartment cell under  $\text{N}_2$  using a 3 mm diameter glassy carbon electrode as the working electrode, platinum wire purchased from Alfa Aesar as the auxiliary electrode, and silver wire as the reference electrode. Ferrocene was used as an internal standard in all electrochemical experiments. Electrochemical experiments were carried out in either 0.1 M  $\text{TBAPF}_6$   $\text{CH}_3\text{CN}$  solutions or 0.1 M  $\text{KNO}_3$  1:1  $\text{CH}_3\text{CN}:\text{H}_2\text{O}$  solutions.

Controlled potential electrolysis experiments were carried out in a two-chambered H-cell. The first chamber held the working and reference electrodes in 50 mL of 0.5 mM  $[\text{Co}(\text{bds})_2][n\text{Bu}_4\text{N}]$  in 0.1 M  $\text{KNO}_3$  1:1  $\text{MeCN}:\text{H}_2\text{O}$  solution. The second chamber contained the counter electrode in 25 mL of 0.1 M  $\text{KNO}_3$  1:1  $\text{MeCN}:\text{H}_2\text{O}$  solution. The two chambers were separated from each by a fine porosity frit. The reference electrode was placed in a separate compartment and connected by a Vycor frit. Glassy carbon plate electrodes (6 cm  $\times$  1 cm  $\times$  0.3 cm; Tokai Carbon USA) were used as the working and auxiliary electrodes. Ferrocene was used as an internal standard for all controlled potential electrolysis experiments. Using a gas-tight syringe, 2 mL of gas were withdrawn from the headspace of the H cell and injected into a gas chromatography instrument (Shimadzu GC-2010-Plus) equipped with a BID detector and a Restek ShinCarbon ST Micropacked column. To determine the Faradaic efficiency, the theoretical  $\text{H}_2$  amount based on total charge flowed is compared with the GC-detected  $\text{H}_2$  produced from controlled-potential electrolysis.

### Physical Methods

UV-Vis spectra were taken using a UV-1800 Shimadzu UV spectrophotometer and quartz cuvettes.

FT-IR spectra were acquired using a Bruker Vertex 80v spectrometer. Samples (2 mg) for analysis were mixed into a KBr (100 mg) matrix and pressed into pellets.

XPS data were collected using a Kratos AXIS Ultra instrument. The monochromatic X-ray source was the Al K  $\alpha$  line at 1486.6 eV, directed at 35° to the sample surface (55° off normal).

Emitted photoelectrons were collected at an angle of 35° with respect to the sample surface (55° off normal) by a hemispherical analyzer. The angle between the electron collection lense and X-ray source is 71°. Low-resolution survey spectra were acquired between binding energies of 1–1200 eV. Higher-resolution detailed scans, with a resolution of ~0.1 eV, were collected on individual XPS lines of interest. The sample chamber was maintained at  $< 2 \times 10^{-9}$  Torr. The XPS data were analyzed using the CasaXPS software.

### Computational Methods

All calculations were run using the *Q-CHEM* program package.<sup>[2]</sup> Geometry optimizations were run with unrestricted DFT calculations at the  $\omega$ -B97x-D level of theory using a relatively small 6-31+G\* basis for a low-cost analysis of the system, and were verified as stable geometries with frequency calculations at the same level of theory. All single-point energy calculations were carried out in the 6-31++G\*\* basis, with additional polarization functions and further augmentation. The  $\omega$ -B97x-D functional was used throughout this study, as it provides reduced self-interaction errors through long-range Hartree-Fock corrections and some empirical fitting for accuracy, which is beneficial for determining the ionization potentials of transition metal-containing systems.

Solvation effects were considered for redox potential analysis with the conductor-like screening model (COSMO).<sup>[3]</sup> Solvation effects were considered for a 1:1 mixture of acetonitrile:water (using a dielectric constant of 50.15), as this is a convenient solvent for the dissolution and electrochemical characterization of  $[\text{Co}(\text{bds})_2]^-$ . The redox potential of the species was determined through calculation of the Gibbs free energy for the gas-phase ionization process.<sup>[4]</sup> This was achieved through a simple Hess cycle calculation using the adiabatic ionization energy of the dianionic species (calculated by the  $\Delta$ SCF procedure) as well as the solvation energies of the oxidized and reduced species. All calculated redox potentials are presented with respect to the ferrocene/ferrocenium couple for straightforward comparison between calculated potentials and electrochemical measurements. The standard accepted values of 4.281 V for SHE and 0.400 V vs SHE for the  $\text{Fc}/\text{Fc}^+$  couple were applied for referencing of absolute potentials. Spin density plots were generated as implemented in the QChem software package for a visualization of spin distribution across the metal site and redox non-innocent ligands.<sup>[5]</sup>

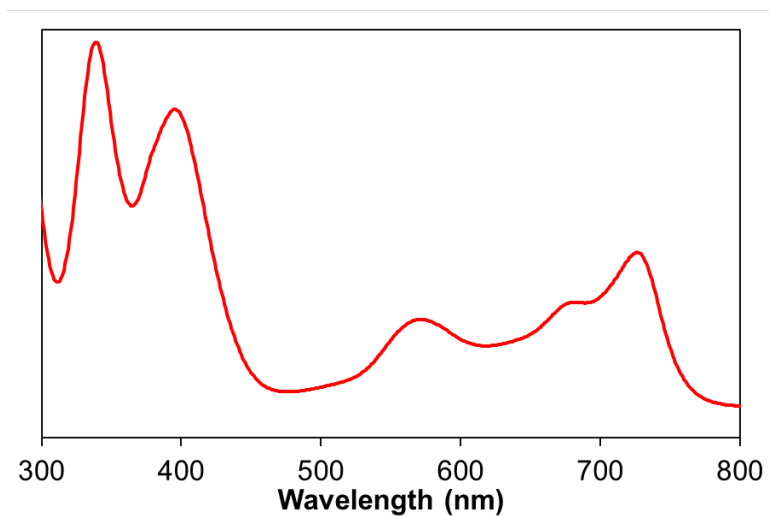


**Figure S1.** UV-Vis absorption spectra of [Co(bds)<sub>2</sub>]<sup>-</sup> in acetonitrile.

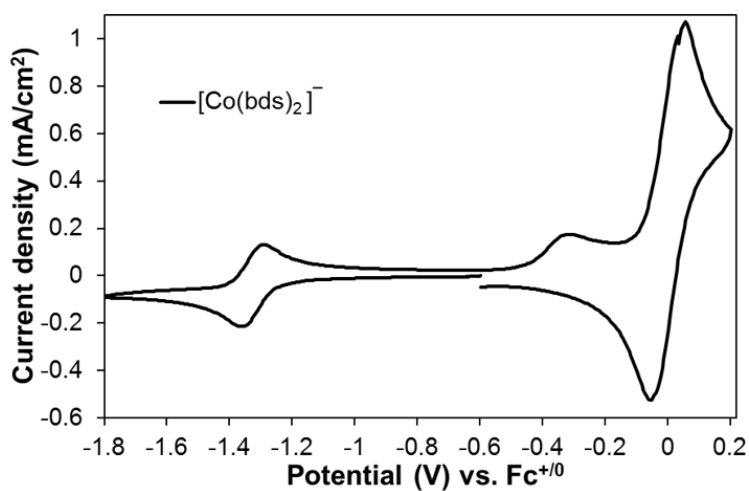


**Figure S2.** Cyclic voltammogram of [Co(bds)<sub>2</sub>]<sup>-</sup> (0.5 mM) in acetonitrile with 0.1 M TBAPF<sub>6</sub> at a scan rate of 100 mV/s. Ferrocene is used as an internal standard. An irreversible feature is seen upon oxidation of [Co(bds)<sub>2</sub>]<sup>-</sup> at -0.32 V vs. Fc<sup>+0</sup> indicating the low chemical stability of oxidized [Co(bds)<sub>2</sub>]<sup>-</sup>. A similar irreversible feature upon oxidation is observed for [Co(bdt)<sub>2</sub>]<sup>-</sup> in acetonitrile and dichloromethane solutions.<sup>[6]</sup>

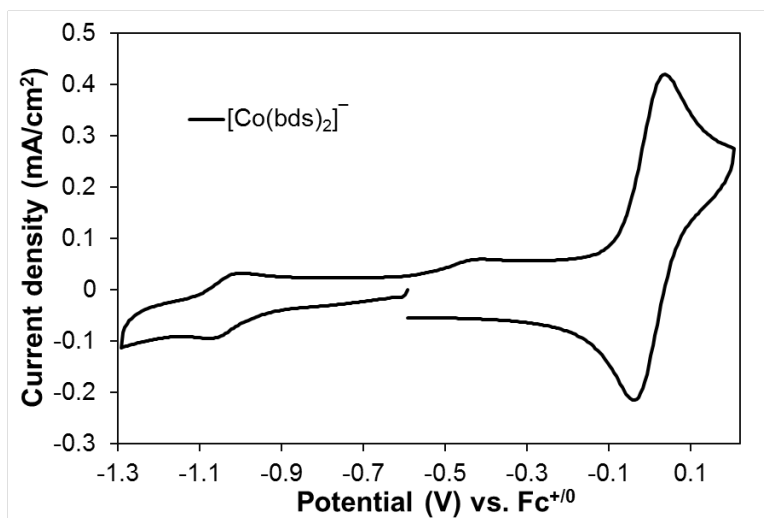


**Figure S3.** Cyclic voltammogram of  $[\text{Co}(\text{bds})_2]^-$  (0.5 mM) in 1:1  $\text{CH}_3\text{CN}:\text{H}_2\text{O}$  with 0.1 M  $\text{KNO}_3$  at a scan rate of 100 mV/s. Ferrocene is used as an internal standard.

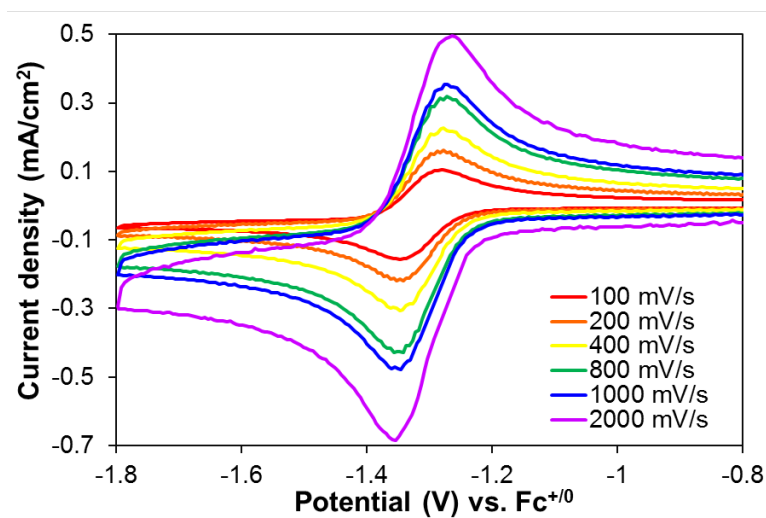


**Figure S4.** Cyclic voltammograms of  $[\text{Co}(\text{bds})_2]^-$  (0.5 mM) in acetonitrile with 0.1 M  $\text{TBAPF}_6$  at scan rates ranging from 100 mV/s (red) to 2000 mV/s (purple).

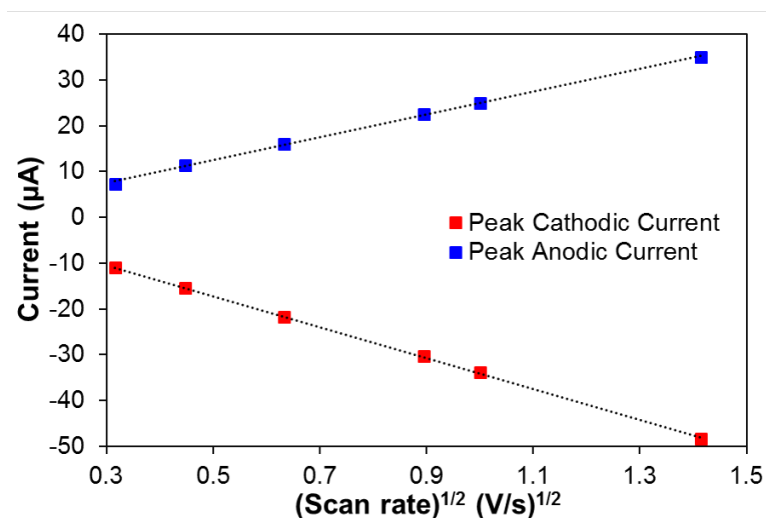


**Figure S5.** Cathodic peak current (red) and anodic peak current (blue) as a function of the square root of the scan rate. The peak currents were obtained from cyclic voltammograms of  $[\text{Co}(\text{bds})_2]^-$  (0.5 mM) in acetonitrile with 0.1 M  $\text{TBAPF}_6$  at scan rates ranging from 100 mV/s to 2000 mV/s.

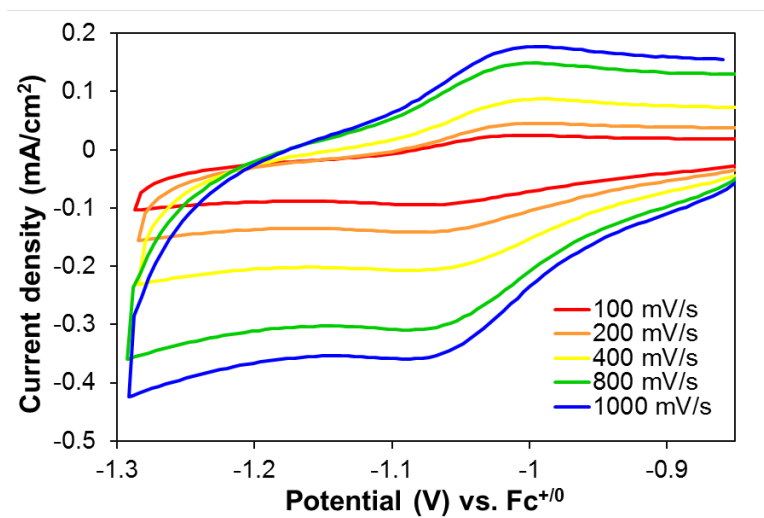


**Figure S6.** Cyclic voltammograms of  $[\text{Co}(\text{bds})_2]^-$  (0.5 mM) in 1:1  $\text{CH}_3\text{CN}:\text{H}_2\text{O}$  with 0.1 M  $\text{KNO}_3$  at scan rates ranging from 100 mV/s (red) to 1000 mV/s (blue).

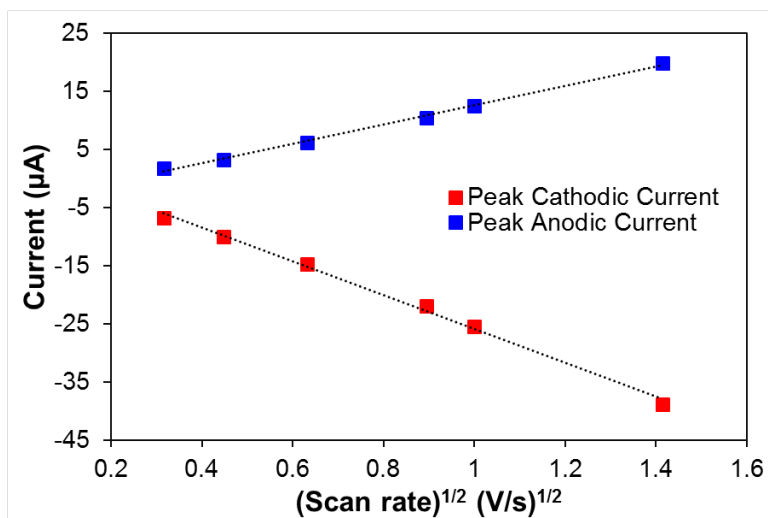


**Figure S7.** Cathodic peak current (red) and anodic peak current (blue) as a function of the square root of the scan rate. The cathodic and anodic peak currents increase linearly as a function of the square root of the scan rate. The linear fits of the data suggest that the species are freely diffusing in solution. The peak currents were obtained from cyclic voltammograms of  $[\text{Co}(\text{bds})_2]^-$  (0.5 mM) in 1:1  $\text{CH}_3\text{CN}:\text{H}_2\text{O}$  with 0.1 M  $\text{KNO}_3$  at scan rates ranging from 100 mV/s to 2000 mV/s.

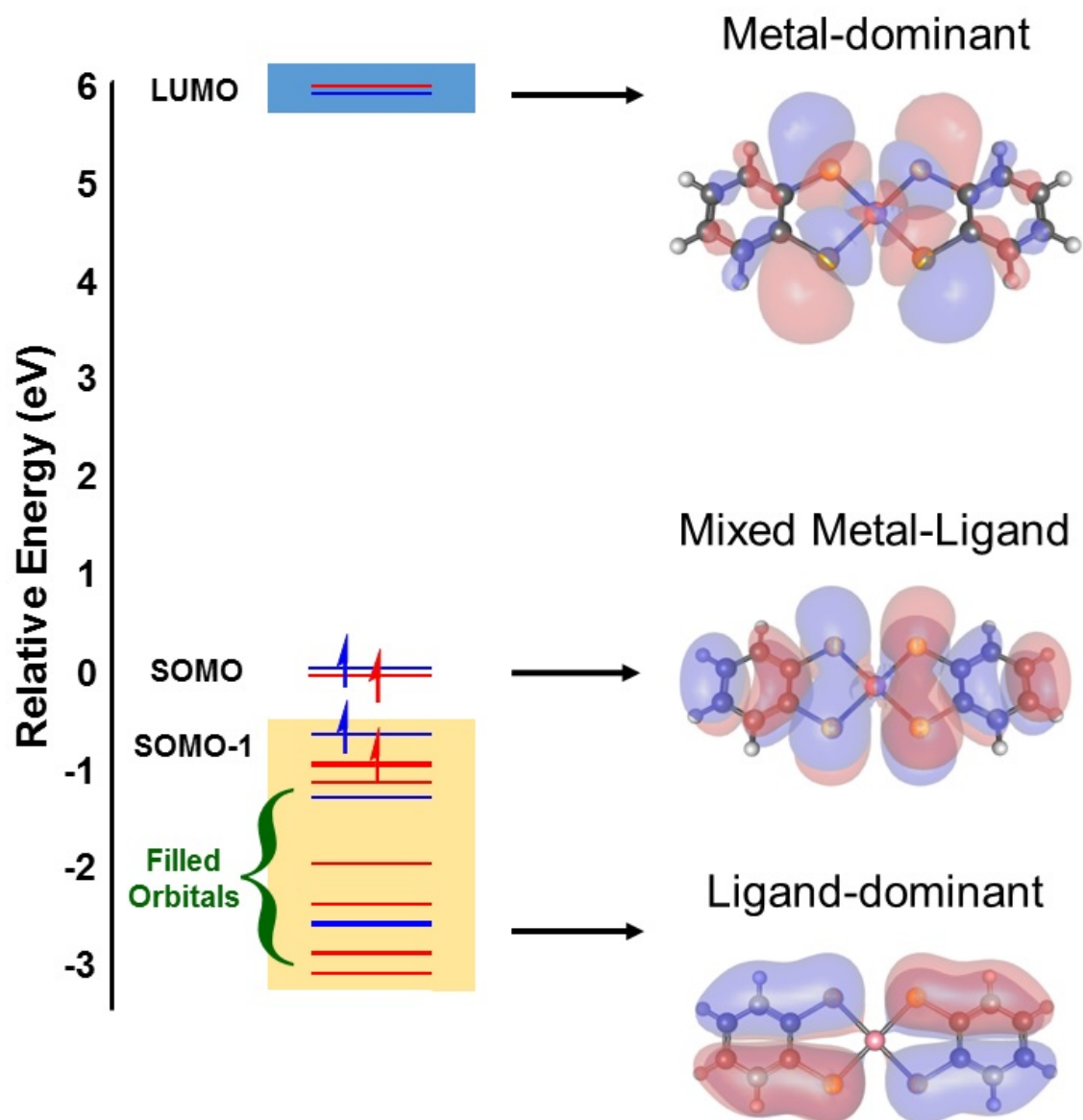


**Figure S8.** Relative molecular orbital energies of  $[\text{Co}(\text{bds})_2]^-$  (blue) versus  $[\text{Co}(\text{bdt})_2]^-$  (red) (where bdt = 1,2-benzenedithiolate).

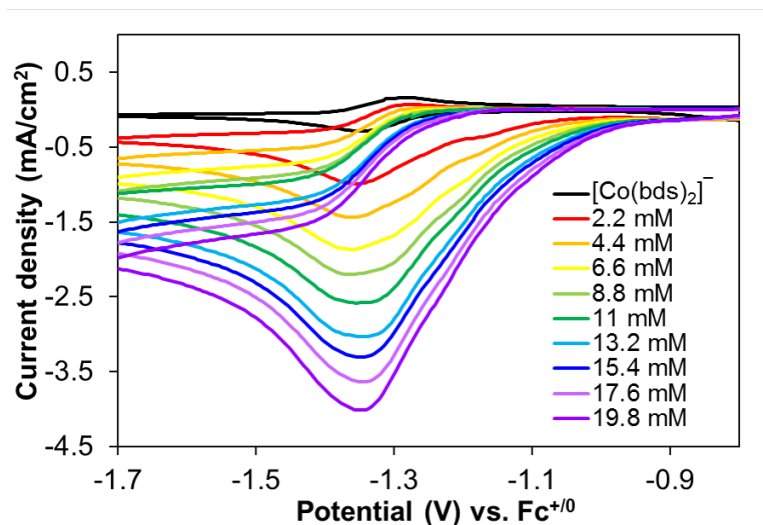


**Figure S9.** Cyclic voltammograms of  $[\text{Co}(\text{bds})_2]^-$  (0.5 mM) in acetonitrile with 0.1 M  $\text{TBAPF}_6$  at varying concentrations of trifluoroacetic acid. Scan rate: 100 mV/s.

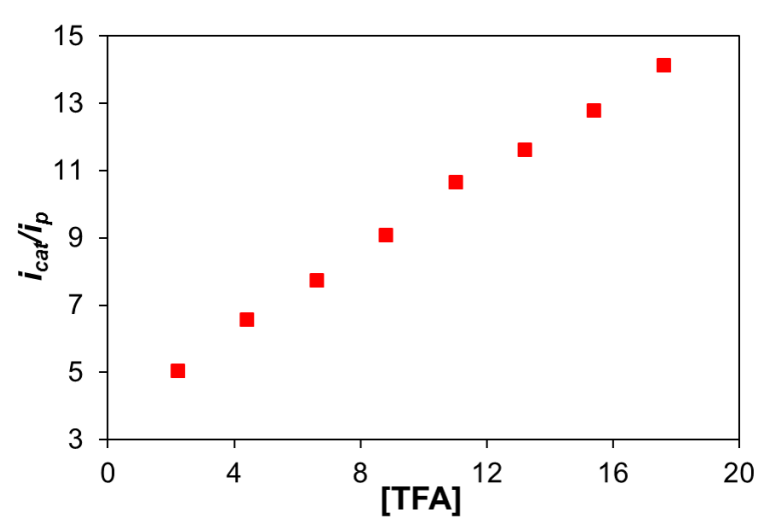


**Figure S10.** Plot of  $i_{\text{cat}}/i_p$  versus the concentration of trifluoroacetic acid taken at 100 mV/s in acetonitrile with 0.1 M  $\text{TBAPF}_6$  and 0.5 mM of  $[\text{Co}(\text{bds})_2]^-$ . Saturation is not achieved because of the formation of a black precipitate at high acid concentrations.

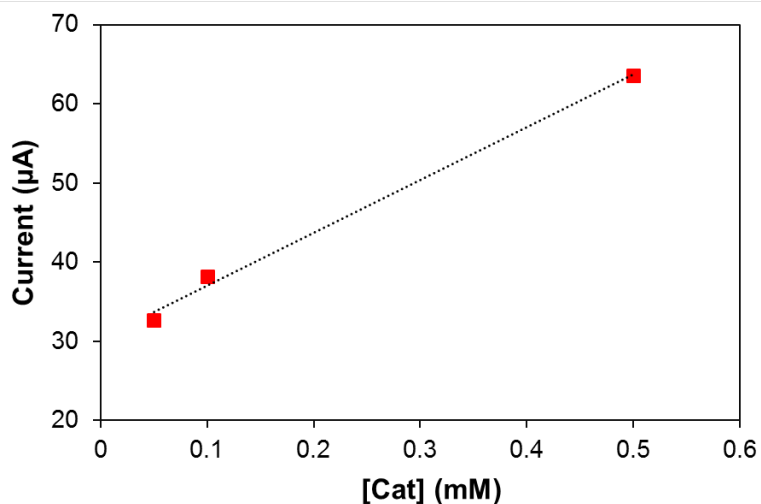


**Figure S11.** Plot of maximum current measured at  $-1.35$  V vs.  $\text{Fc}^{+/0}$  versus catalyst concentration during cyclic voltammograms of  $[\text{Co}(\text{bds})_2]^-$  in  $0.1$  M  $\text{TBAPF}_6$  in  $\text{CH}_3\text{CN}$  in the presence of trifluoroacetic acid ( $2.2$  mM).

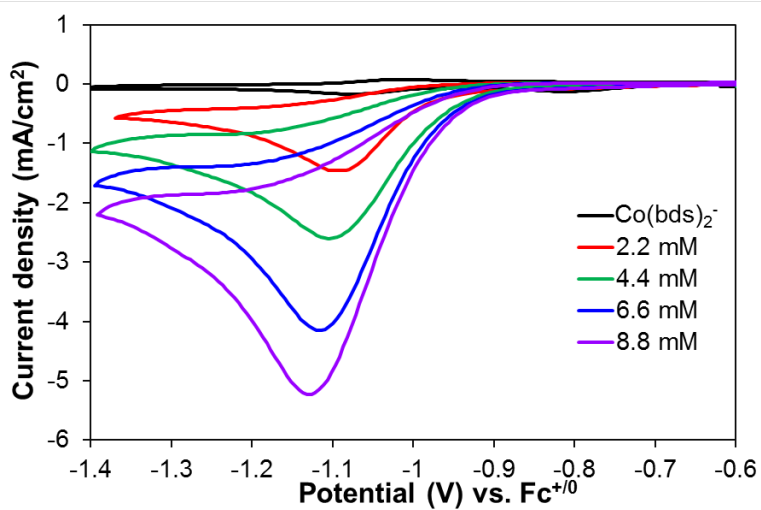


**Figure S12.** Cyclic voltammograms of  $[\text{Co}(\text{bds})_2]^-$  ( $0.5$  mM) in  $1:1$   $\text{CH}_3\text{CN}:\text{H}_2\text{O}$  with  $0.1$  M  $\text{KNO}_3$  at varying concentrations of trifluoroacetic acid. Scan rate:  $100$  mV/s.

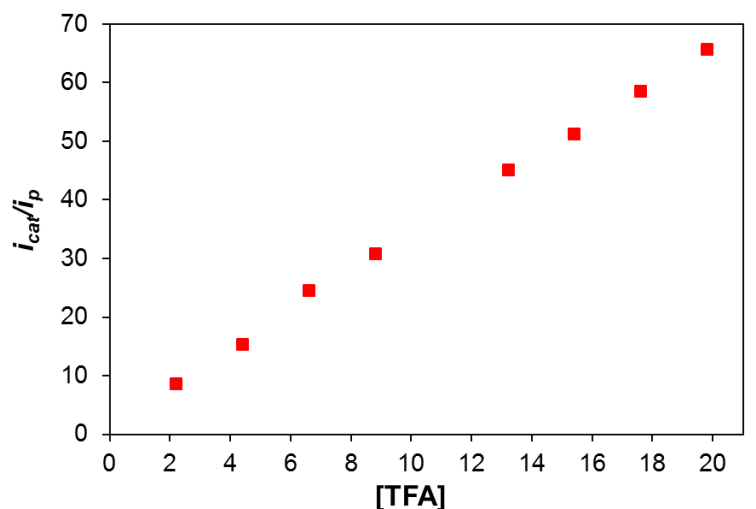


**Figure S13.** Plot of  $i_{cat}/i_p$  versus the concentration of trifluoroacetic acid taken at 100 mV/s in 1:1 CH<sub>3</sub>CN:H<sub>2</sub>O with 0.1 M KNO<sub>3</sub> and 0.5 mM of [Co(bds)<sub>2</sub>]<sup>-</sup>. Saturation is not achieved because of the formation of a black precipitate at high acid concentrations.

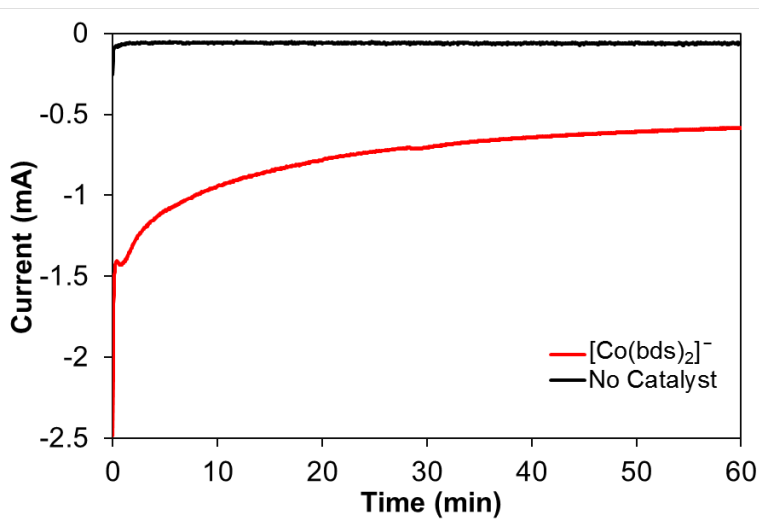


**Figure S14.** Controlled potential electrolysis (CPE) of 0.5 mM [Co(bds)<sub>2</sub>]<sup>-</sup> (red) and with no catalyst (black) in 0.1 M KNO<sub>3</sub> 1:1 MeCN:H<sub>2</sub>O solution and 8.8 mM TFA at -1.02 V vs. Fc<sup>+0</sup>. The decrease in current over time is due to the visual formation of the black precipitate during the CPE experiment.

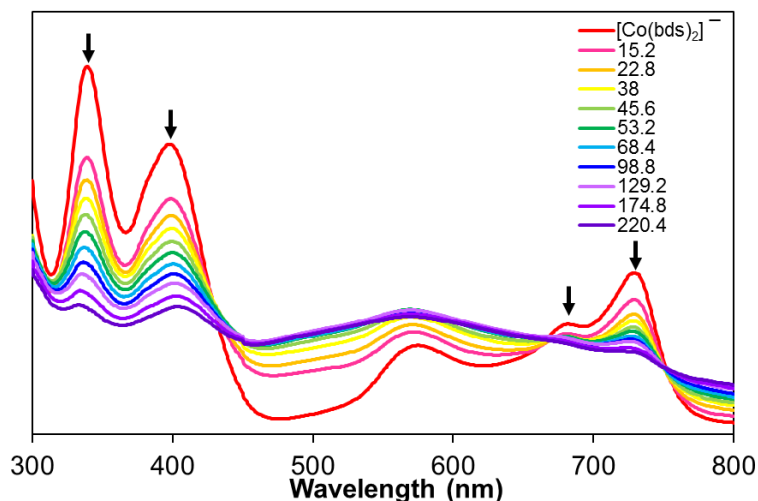


**Figure S15.** UV-Vis absorbance spectra of  $[\text{Co}(\text{bds})_2]^-$  in DMF after the addition of trifluoroacetic acid (15.2  $\mu\text{L}$  – 220.4  $\mu\text{L}$ ) displaying the disappearance of the diagnostic UV-Vis features of  $[\text{Co}(\text{bds})_2]^-$ .

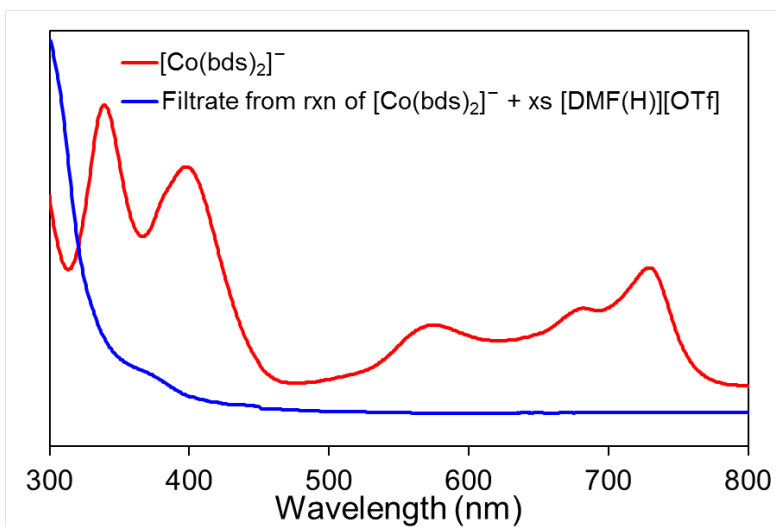


**Figure S16.** UV-Vis absorbance spectra of  $[\text{Co}(\text{bds})_2]^-$  (red) and the remaining acetonitrile solution (blue) after treating  $[\text{Co}(\text{bds})_2]^-$  with  $[\text{DMF}(\text{H})][\text{OTf}]$  to form the black precipitate. The solution was filtered before analysis to remove the black particles. The characteristic UV-Vis features of  $[\text{Co}(\text{bds})_2]^-$  are not observed suggesting complete consumption of  $[\text{Co}(\text{bds})_2]^-$ .

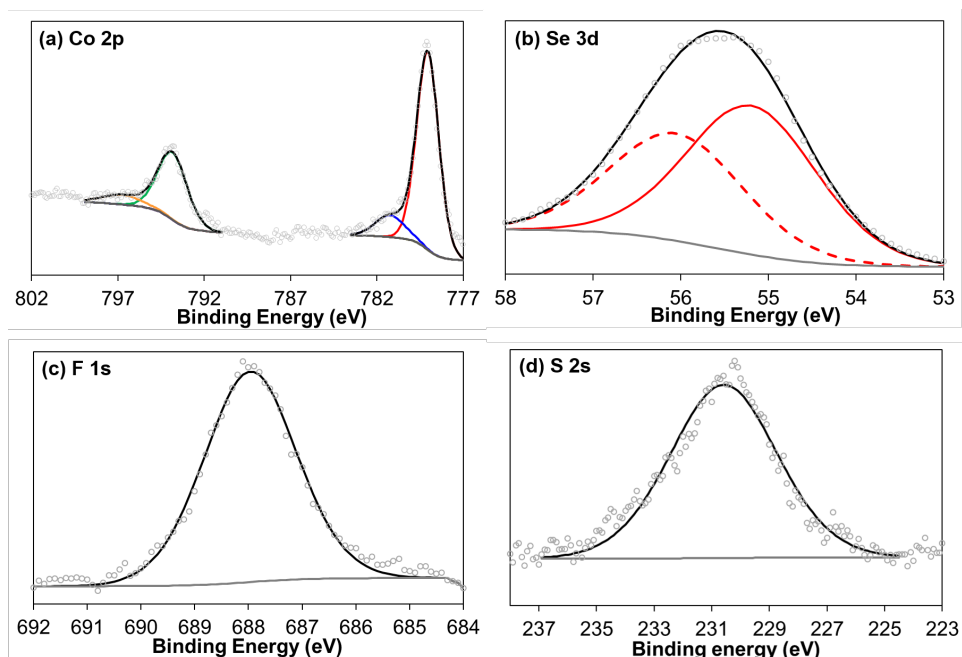


**Figure S17.** X-ray photoelectron spectroscopy analysis of the black precipitate formed from reaction of  $[\text{Co}(\text{bds})_2]^-$  with  $[\text{DMF}(\text{H})][\text{OTf}]$  (a) Co 2p core level XPS spectrum (b) Se 3d core level XPS spectrum (c) F 1s core level XPS spectrum and (d) S 2s core level XPS spectrum.

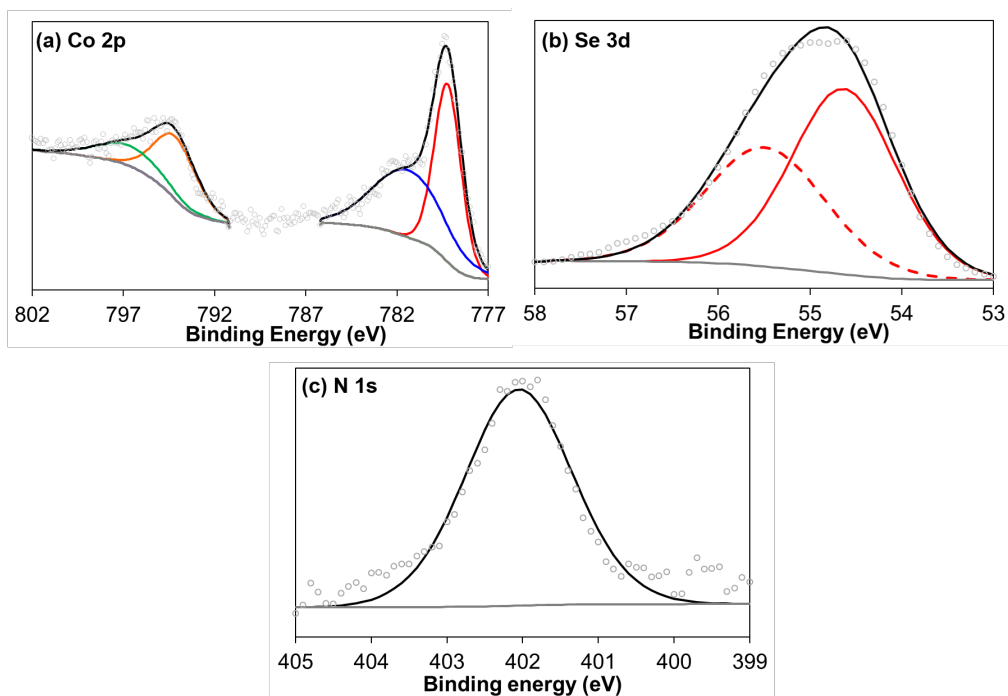


**Figure S18.** X-ray photoelectron spectroscopy of  $[\text{Co}(\text{bds})_2]^-$  (a) Co 2p core level XPS spectrum (b) Se 3d core level XPS spectrum and (c) N 1s core level spectrum.

XPS Region	Binding Energy (eV) for [Co(bds) <sub>2</sub> ][nBu <sub>4</sub> N]	Binding Energy (eV) for Black Precipitate	Δ Binding Energy (eV)
Co 2p <sub>3/2</sub>	779.4	778.9	0.5
Co 2p <sub>1/2</sub>	794.6	794.0	0.6
Se 3d <sub>5/2</sub>	54.6	55.2	-0.6
Se 3d <sub>3/2</sub>	55.5	56.1	-0.6

**Table S1.** Comparison of the XPS binding energies of the Co 2p and Se 3d regions for [Co(bds)<sub>2</sub>][nBu<sub>4</sub>N] and the black precipitate.

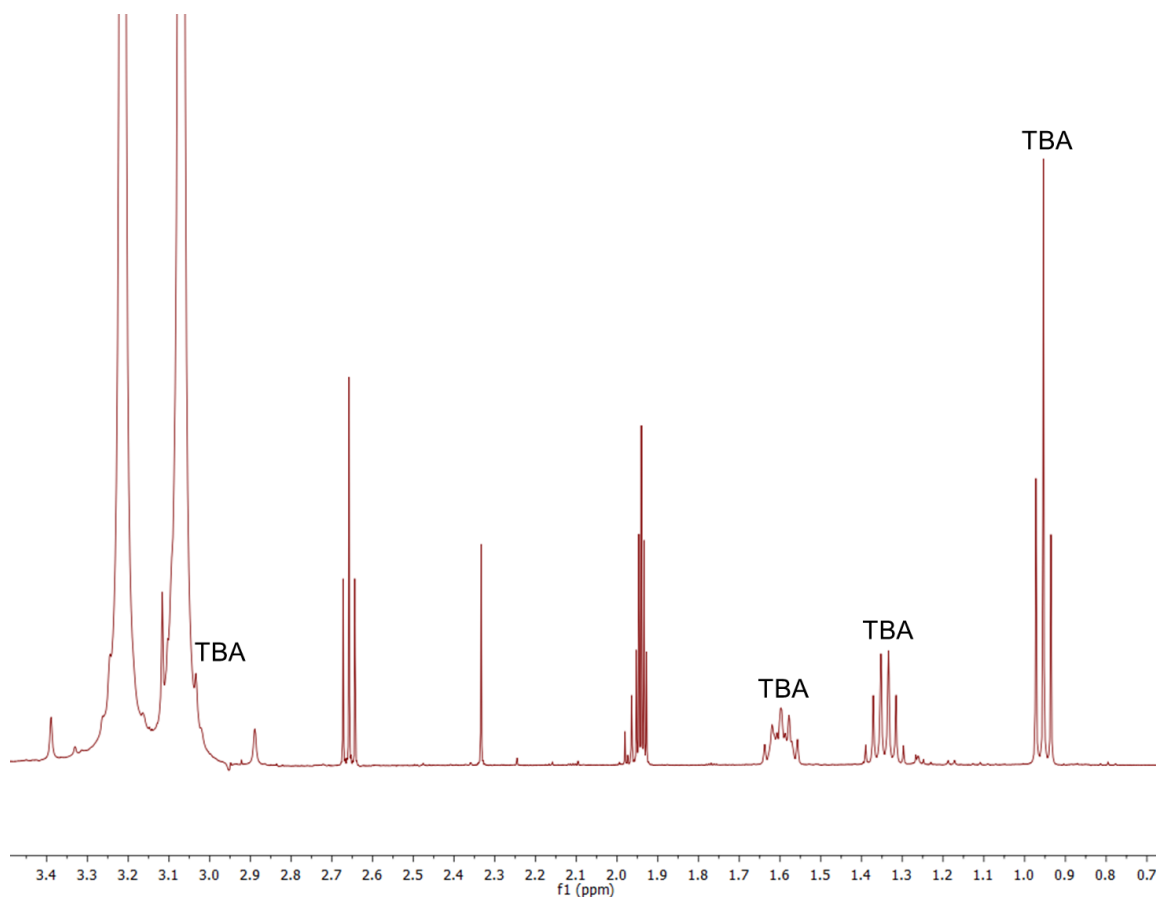


**Figure S19.** <sup>1</sup>H NMR of resultant acetonitrile-*d*<sub>3</sub> solution after the treatment of [Co(bds)<sub>2</sub>]<sup>-</sup> with excess [DMF(H)][OTf]. The generated black precipitate was collected by filtration, and the resultant acetonitrile-*d*<sub>3</sub> solution was analyzed by <sup>1</sup>H NMR spectroscopy. Tetrabutylammonium (TBA) triflate is observed in the resultant solution, confirming the loss of TBA during the formation of the black precipitate. Additional peaks are related to [DMF(H)][OTf] and acetonitrile-*d*<sub>3</sub>.

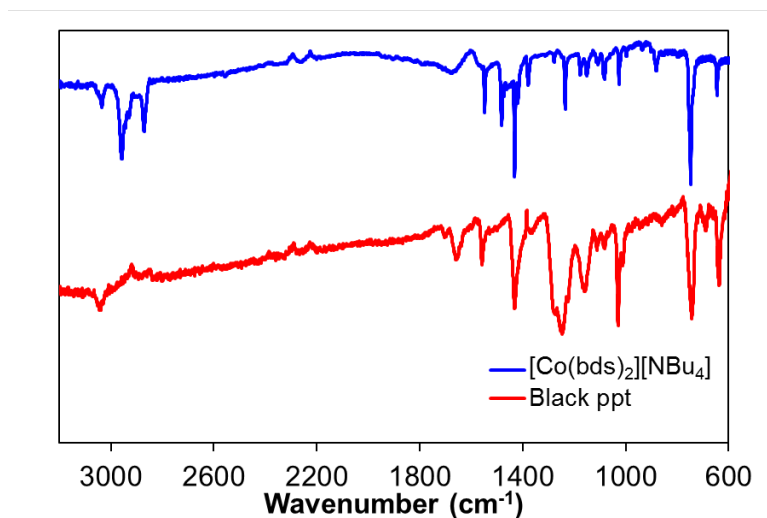


**Figure S20.** FT-IR spectra of [Co(bds)<sub>2</sub>]<sup>-</sup> (blue) and the black precipitate formed in the presence of acid (red).

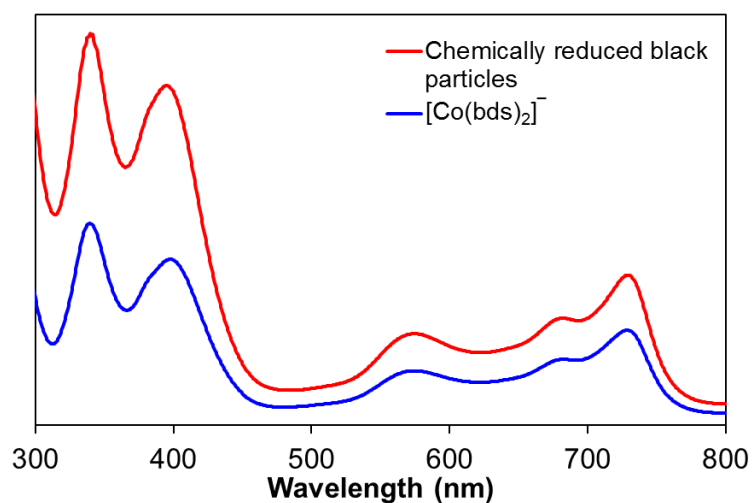


**Figure S21.** UV-Vis absorbance of [Co(bds)<sub>2</sub>]<sup>-</sup> in DMF (blue) and a filtered solution from the reaction of KC<sub>8</sub> and black particles in DMF displaying the regeneration [Co(bds)<sub>2</sub>]<sup>-</sup> upon chemical reduction of the black particles (red).

<u>Complex</u>	<u>Spin</u>	<u>Spin Density</u>	<u>Spin Orbitals</u>
$[\text{Co}(\text{bds})_2]^{-1}$	3		SOMO $\uparrow$ — SOMO-1 $\uparrow$ — $\alpha$ $\beta$
$[\text{Co}(\text{bds})_2]^{-2}$	2		SOMO $\uparrow$ — SOMO-1 $\uparrow$ — $\alpha$ $\beta$
$[\text{Co}(\text{bdt})_2]^{-1}$	3		SOMO $\uparrow$ — SOMO-1 $\uparrow$ — $\alpha$ $\beta$
$[\text{Co}(\text{bdt})_2]^{-2}$	2		SOMO $\uparrow$ — SOMO-1 $\uparrow$ — $\alpha$ $\beta$

**Figure S22.** Spin densities<sup>[5]</sup> of  $[\text{Co}(\text{bds})_2]^{-1}$  and  $[\text{Co}(\text{bdt})_2]^{-1}$  along with their one electron reduced forms,  $[\text{Co}(\text{bds})_2]^{-2}$  and  $[\text{Co}(\text{bdt})_2]^{-2}$ .

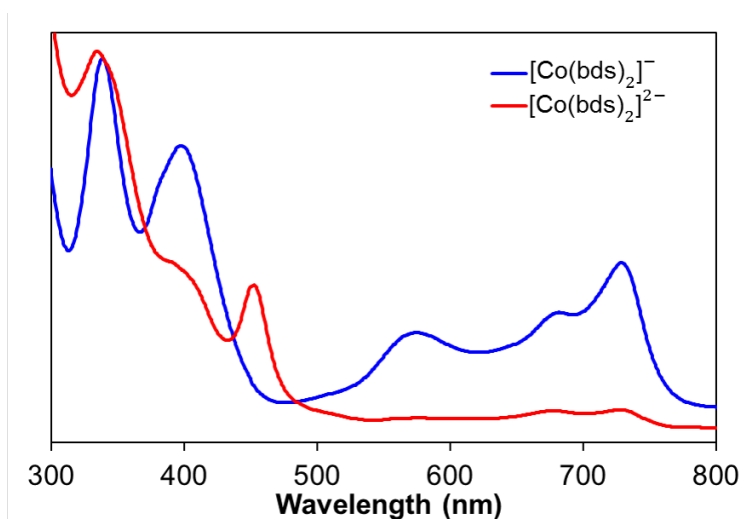


**Figure S23.** UV-Vis absorbance of  $[\text{Co}(\text{bds})_2]^{-1}$  (blue) and  $[\text{Co}(\text{bds})_2]^{-2}$  (red) in DMF.

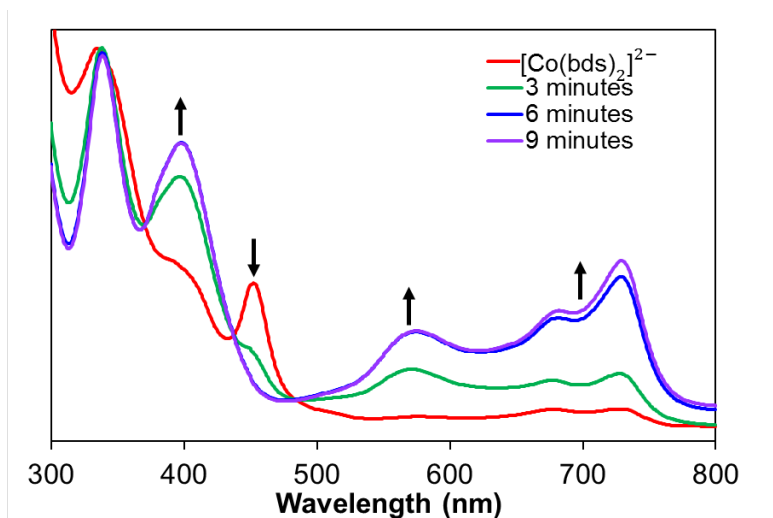


**Figure S24.** UV-Vis absorbance of  $[\text{Co}(\text{bds})_2]^{2-}$  (red) upon exposure to air for 3 (green), 6 (blue), and 9 (purple) minutes depicting regeneration of  $[\text{Co}(\text{bds})_2]^-$ .

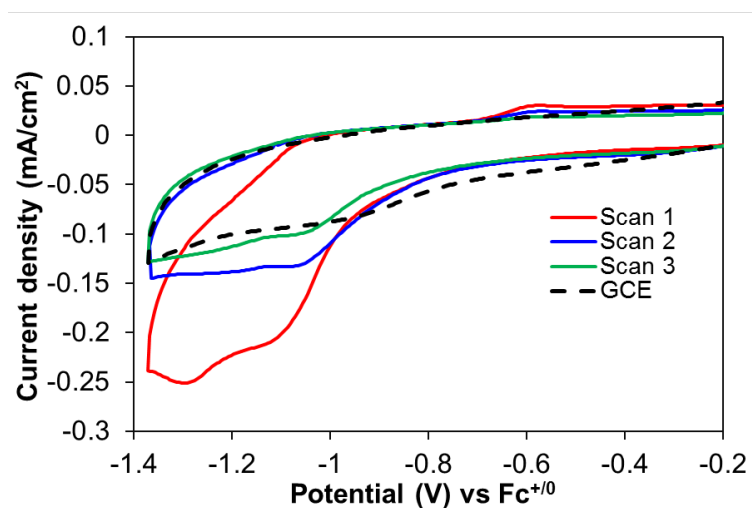


**Figure S25.** Cyclic voltammograms of a glassy carbon electrode soaked for 30 minutes in a solution of  $[\text{Co}(\text{bds})_2]^-$  and excess  $[\text{DMF}(\text{H})][\text{OTf}]$  and a blank glassy carbon electrode (black dashed, GCE) in 1:1 MeCN:H<sub>2</sub>O solution with 0.1 M KNO<sub>3</sub> (scan rate: 100 mV/s). The large current density observed for the first scan (red) indicates removal of the electrode-adsorbed material upon reduction. Subsequent scans display a broad reduction feature, indicative of the formation of the  $[\text{Co}(\text{bds})_2]^-$  units. The drop in current density for sequential scans is attributed to diffusion of  $[\text{Co}(\text{bds})_2]^-$  away from the electrode. Analogous electrochemical behavior of an adsorbed black precipitate has been reported for the cobalt benzenedithiolate complex.<sup>[7]</sup>

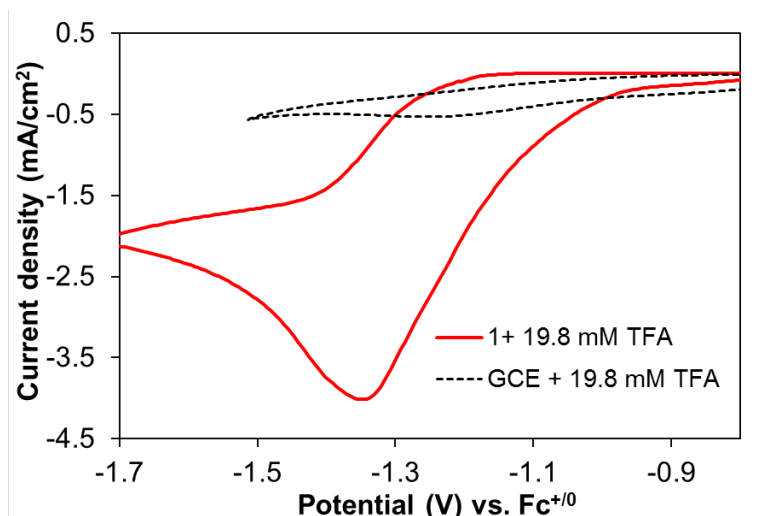


**Figure S26.** Cyclic voltammograms of  $[\text{Co}(\text{bds})_2]^-$  (0.5 mM, red) and a bare glassy carbon electrode (GCE, black dashed) in acetonitrile with 0.1 M  $\text{TBAPF}_6$  and 19.8 mM TFA. Scan rate: 100 mV/s.

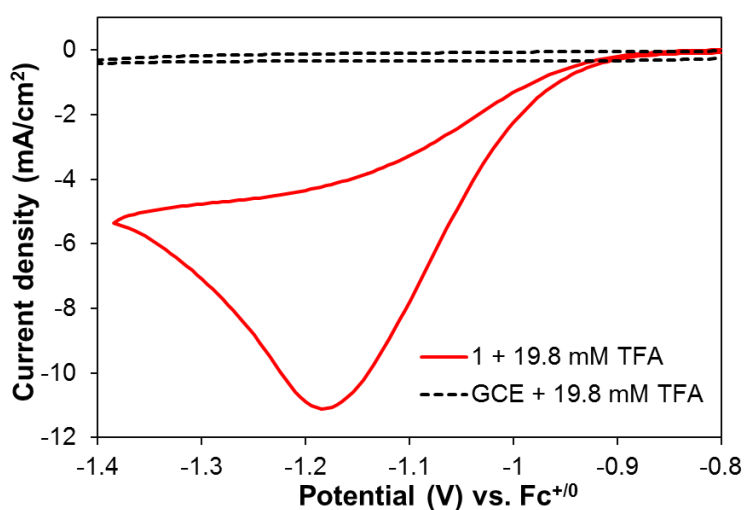


**Figure S27.** Cyclic voltammograms of  $[\text{Co}(\text{bds})_2]^-$  (0.5 mM, red) and a bare glassy carbon electrode (GCE, black dashed) in 1:1  $\text{CH}_3\text{CN}:\text{H}_2\text{O}$  with 0.1 M  $\text{KNO}_3$  and 19.8 mM TFA. Scan rate: 100 mV/s.

### X-ray Structure Determination for 1

The X-ray intensity data were measured on a Bruker APEX DUO system equipped with a multi-layer optics monochromator and a  $\text{CuK}\alpha$  IuS microsource ( $\lambda = 1.54178 \text{ \AA}$ ). The structure was solved and refined using the Bruker SHELXTL Software Package, using the space group  $C 1 2/c 1$ , with  $Z = 4$  for the formula unit,  $\text{C}_{36}\text{H}_{28}\text{CoPSe}_4$ .

A total of 5904 frames were collected. The total exposure time was 23.02 hours. The frames were integrated with the Bruker SAINT software package using a SAINT V8.37A (Bruker AXS, 2013) algorithm. The integration of the data using a monoclinic unit cell yielded a total of 36109 reflections to a maximum  $\theta$  angle of  $68.28^\circ$  ( $0.83 \text{ \AA}$  resolution), of which 2760 were independent (average redundancy 13.083, completeness = 94.7%,  $R_{\text{int}} = 6.54\%$ ,  $R_{\text{sig}} = 2.90\%$ ) and 2538 (91.96%) were greater than  $2\sigma(F^2)$ . The final cell constants of  $a = 16.1283(8) \text{ \AA}$ ,  $b = 12.1688(6) \text{ \AA}$ ,  $c = 16.3580(8) \text{ \AA}$ ,  $\beta = 96.567(3)^\circ$ , volume =  $3189.4(3) \text{ \AA}^3$ , are based upon the refinement of the XYZ-centroids of 9947 reflections above  $20 \sigma(I)$  with  $10.30^\circ < 2\theta < 136.4^\circ$ . Data were corrected for absorption effects using the multi-scan method (SADABS). The ratio of minimum to maximum apparent transmission was 0.726. The calculated minimum and maximum transmission coefficients (based on crystal size) are 0.2970 and 0.7000.

The structure was solved and refined using the Bruker SHELXTL Software Package, using the space group  $C 1 2/c 1$ , with  $Z = 4$  for the formula unit,  $C_{36}H_{28}CoPSe_4$ . The final anisotropic full-matrix least-squares refinement on  $F^2$  with 192 variables converged at  $R_1 = 2.32\%$ , for the observed data and  $wR_2 = 5.63\%$  for all data. The goodness-of-fit was 1.037. The largest peak in the final difference electron density synthesis was  $0.369 \text{ e}^-/\text{\AA}^3$  and the largest hole was  $-0.376 \text{ e}^-/\text{\AA}^3$  with an RMS deviation of  $0.076 \text{ e}^-/\text{\AA}^3$ . On the basis of the final model, the calculated density was  $1.804 \text{ g/cm}^3$  and  $F(000)$ , 1688  $e^-$ .

**Table S2.** Crystal data and structure refinement for **1<sup>TPP</sup>**.

Chemical formula	$C_{36}H_{28}CoPSe_4$	
Formula weight	866.32 g/mol	
Temperature	100(2) K	
Wavelength	1.54178 $\text{\AA}$	
Crystal size	$0.038 \times 0.070 \times 0.159 \text{ mm}$	
Crystal habit	dark brown blade	
Crystal system	monoclinic	
Space group	$C 1 2/c 1$	
Unit cell dimensions	$a = 16.1283(8) \text{ \AA}$	$\alpha = 90^\circ$
	$b = 12.1688(6) \text{ \AA}$	$\beta = 96.567(3)^\circ$
	$c = 16.3580(8) \text{ \AA}$	$\gamma = 90^\circ$
Volume	$3189.4(3) \text{ \AA}^3$	
Z	4	
Density (calculated)	$1.804 \text{ g/cm}^3$	
Absorption coefficient	$10.100 \text{ mm}^{-1}$	
$F(000)$	1688	
Diffractionmeter	Bruker APEX DUO	
Radiation source	IuS microsource, $CuK\alpha$	
Theta range for data collection	$4.56$ to $70.32^\circ$	
Index ranges	$-19 \leq h \leq 19$ , $-14 \leq k \leq 14$ , $-19 \leq l \leq 19$	
Reflections collected	41906	

Independent reflections	3036 [R(int) = 0.0653]
Coverage of independent reflections	99.7%
Absorption correction	multi-scan
Max. and min. transmission	0.7000 and 0.2970
Structure solution technique	direct methods
Structure solution program	SHELXTL XT 2014/5 (Bruker AXS, 2014)
Refinement method	Full-matrix least-squares on F <sup>2</sup>
Refinement program	SHELXTL XL 2014/7 (Bruker AXS, 2014)
Function minimized	$\Sigma w(F_o^2 - F_c^2)^2$
Data / restraints / parameters	3039 / 0 / 192
Goodness-of-fit on F <sup>2</sup>	1.038
$\Delta/\sigma_{max}$	0.002
Final R indices	2799 data; $I > 2\sigma(I)$ $R_1 = 0.0234$ , $wR_2 = 0.0551$ all data $R_1 = 0.0268$ , $wR_2 = 0.0569$
Weighting scheme	$w = 1/[\sigma^2(F_o^2) + (0.0295P)^2 + 4.0287P]$ where $P = (F_o^2 + 2F_c^2)/3$
Largest diff. peak and hole	0.344 and -0.402 eÅ <sup>-3</sup>
R.M.S. deviation from mean	0.077 eÅ <sup>-3</sup>

**Table S3. Bond lengths (Å) for 1<sup>TPP</sup>.**

C1-C2	1.388(3)	C1-C6	1.402(3)
C1-Se1	1.908(2)	C2-C3	1.394(3)
C2-Se2	1.912(2)	C3-C4	1.383(4)
C3-H3	0.95	C4-C5	1.387(4)
C4-H4	0.95	C5-C6	1.386(4)
C5-H5	0.95	C6-H6	0.95
C7-C12	1.388(3)	C7-C8	1.398(3)
C7-P1	1.796(2)	C8-C9	1.386(3)
C8-H8	0.95	C9-C10	1.385(4)
C9-H9	0.95	C10-C11	1.382(4)
C10-H10	0.95	C11-C12	1.392(4)
C11-H11	0.95	C12-H12	0.95
C13-C18	1.395(3)	C13-C14	1.397(3)
C13-P1	1.794(2)	C14-C15	1.388(3)
C14-H14	0.95	C15-C16	1.383(4)
C15-H15	0.95	C16-C17	1.387(4)
C16-H16	0.95	C17-C18	1.390(3)
C17-H17	0.95	C18-H18	0.95
Co1-Se2	2.2868(2)	Co1-Se2	2.2869(2)
Co1-Se1	2.2921(2)	Co1-Se1	2.2922(2)
P1-C13	1.794(2)	P1-C7	1.796(2)

**Table S4. Bond angles (°) for 1<sup>TPP</sup>.**

C2-C1-C6	119.6(2)	C2-C1-Se1	120.54(17)
C6-C1-Se1	119.81(19)	C1-C2-C3	120.1(2)
C1-C2-Se2	119.31(17)	C3-C2-Se2	120.64(17)
C4-C3-C2	120.0(2)	C4-C3-H3	120.0
C2-C3-H3	120.0	C3-C4-C5	120.3(2)
C3-C4-H4	119.9	C5-C4-H4	119.9
C4-C5-C6	120.6(2)	C4-C5-H5	119.9
C6-C5-H5	119.9	C5-C6-C1	119.9(2)
C5-C6-H6	120.1	C1-C6-H6	120.1
C12-C7-C8	120.6(2)	C12-C7-P1	120.90(18)
C8-C7-P1	117.89(17)	C9-C8-C7	119.3(2)
C9-C8-H8	120.4	C7-C8-H8	120.4
C10-C9-C8	120.1(2)	C10-C9-H9	120.0
C8-C9-H9	120.0	C11-C10-C9	120.6(2)
C11-C10-H10	119.7	C9-C10-H10	119.7
C10-C11-C12	119.9(2)	C10-C11-H11	120.0
C12-C11-H11	120.0	C7-C12-C11	119.4(2)
C7-C12-H12	120.3	C11-C12-H12	120.3
C18-C13-C14	120.4(2)	C18-C13-P1	119.47(17)
C14-C13-P1	119.07(18)	C15-C14-C13	119.5(2)
C15-C14-H14	120.2	C13-C14-H14	120.2
C16-C15-C14	119.9(2)	C16-C15-H15	120.0
C14-C15-H15	120.0	C15-C16-C17	120.7(2)
C15-C16-H16	119.7	C17-C16-H16	119.7
C16-C17-C18	120.1(2)	C16-C17-H17	120.0
C18-C17-H17	120.0	C17-C18-C13	119.4(2)
C17-C18-H18	120.3	C13-C18-H18	120.3
Se2-Co1-Se2	180.0	Se2-Co1-Se1	92.008(8)
Se2-Co1-Se1	87.991(9)	Se2-Co1-Se1	87.991(9)
Se2-Co1-Se1	92.010(9)	Se1-Co1-Se1	179.999(12)
C13-P1-C13	111.38(15)	C13-P1-C7	112.37(10)
C13-P1-C7	105.95(10)	C13-P1-C7	105.94(10)
C13-P1-C7	112.37(10)	C7-P1-C7	108.92(15)
C1-Se1-Co1	103.78(7)	C2-Se2-Co1	104.30(7)

**Table S5. Calculated versus experimental bond lengths (Å).**

Bond	Calculated Length	Experimental Length
C1 Se1	1.9071	1.908(2)
C2 Se2	1.9075	1.912(2)
Co Se1	2.31597	2.2921(2)
Co Se2	2.31559	2.2868(2)
Co Se1	2.31589	2.2921(2)
Co Se2	2.31586	2.2869(2)

**Table S6. Calculated versus experimental bond angles (°)**

Bond Angle	Calculated (°)	Experimental (°)
Se2 Co Se2	179.322	180.0
Se2 Co Se1	87.8362	87.991(9)
Se2 Co Se1	92.18973	92.010(9)
Se2 Co Se1	92.1856	92.008(8)
Se2 Co Se1	87.7923	87.991(9)
Se1 Co Se1	179.679	179.999(12)

**References:**

- [1] D. J. Sandman, G. W. Allen, L. A. Acampora, J. C. Stark, S. Jansen, M. T. Jones, G. J. Ashwell, B. M. Foxman, *Inorganic Chemistry* **1987**, *26*, 1664-1669.
- [2] Y. Shao, L. F. Molnar, Y. Jung, J. Kussmann, C. Ochsenfeld, S. T. Brown, A. T. B. Gilbert, L. V. Slipchenko, S. V. Levchenko, D. P. O'Neill, R. A. DiStasio Jr, R. C. Lochan, T. Wang, G. J. O. Beran, N. A. Besley, J. M. Herbert, C. Yeh Lin, T. Van Voorhis, S. Hung Chien, A. Sodt, R. P. Steele, V. A. Rassolov, P. E. Maslen, P. P. Korambath, R. D. Adamson, B. Austin, J. Baker, E. F. C. Byrd, H. Dachsel, R. J. Doerksen, A. Dreuw, B. D. Dunietz, A. D. Dutoi, T. R. Furlani, S. R. Gwaltney, A. Heyden, S. Hirata, C.-P. Hsu, G. Kedziora, R. Z. Khalliulin, P. Klunzinger, A. M. Lee, M. S. Lee, W. Liang, I. Lotan, N. Nair, B. Peters, E. I. Proynov, P. A. Pieniazek, Y. Min Rhee, J. Ritchie, E. Rosta, C. David Sherrill, A. C. Simmonett, J. E. Subotnik, H. Lee Woodcock III, W. Zhang, A. T. Bell, A. K. Chakraborty, D. M. Chipman, F. J. Keil, A.

- Warshel, W. J. Hehre, H. F. Schaefer III, J. Kong, A. I. Krylov, P. M. W. Gill, M. Head-Gordon, *Physical Chemistry Chemical Physics* **2006**, *8*, 3172-3191.
- [3] A. V. Marenich, C. J. Cramer, D. G. Truhlar, *Journal of Chemical Theory and Computation* **2013**, *9*, 609-620; A. Klamt, G. Schuurmann, *Journal of the Chemical Society, Perkin Transactions 2* **1993**, 799-805.
- [4] K. M. Solntsev, D. Ghosh, A. Amador, M. Josowicz, A. I. Krylov, *Journal of Physical Chemistry Letters* **2011**, *2*, 2593-2597.
- [5] A. Ghosh, *JBIC Journal of Biological Inorganic Chemistry* **2006**, *11*, 712-724.
- [6] W. R. McNamara, Z. Han, P. J. Alperin, W. W. Brennessel, P. L. Holland, R. Eisenberg, *Journal of the American Chemical Society* **2011**, *133*, 15368-15371; P. Machata, P. Herich, K. Lušpai, L. Bucinsky, S. Šoralová, M. Breza, J. Kozisek, P. Rapta, *Organometallics* **2014**, *33*, 4846-4859.
- [7] K. J. Lee, B. D. McCarthy, E. S. Rountree, J. L. Dempsey, *Inorganic Chemistry* **2017**, *56*, 1988-1998.